PAPER

Synthesis and characterization of a new monometallic layered double hydroxide using manganese†

Damien Cornu, [ID] *[a] Romain Coustel, [ID] [a] Guillaume Renaudin, [ID] [b]
Guillaume Rogez, [ID] [c] Aurélien Renard,[a] Pierrick Durand,[d] Cédric Carteret [ID] [a] and
Christian Ruby [ID] *[a]

This article reports for the first time the synthesis of an LDH using only manganese as the divalent and tri-valent metallic ion. Analysis of the pH, redox potential, and chemical composition during the oxidation of a manganese basic salt using persulfate indicates the oxidation of 1/3 of the initial Mn^{II} ions, in agreement with the paramagnetic structure and XPS analysis. Infrared, Raman spectra and thermogravimetric analysis results were similar to the ones obtained with Fe-LDH also known as green rust. X-Ray diffractograms and Rietveld refinement were used to determine the structure of this solid. Thermodynamic considerations predict that this solid could reduce nitrate into gaseous nitrogen without further reduction to ammonium or ammonia unlike what is observed for Fe-LDH.

Introduction

Layered double hydroxides (LDHs) or anionic clays are a class of ionic solids with a layered structure and a general formula $[M^{II}_{1-x}M^{III}_x(OH)_2]^{x+}[(A^{n-})_{x/n} mH_2O]^{x-}\cdot$ in which M^{II} and M^{III} are metallic cations and A^{n-} is an intercalated anion. These materials are useful structures for many applications, *e.g.*, catalysis (oxygen evolution reaction[1] and photodegradation of pollutants[2]), anionic exchange[3] or biomedical applications.[4] They are usually synthesized using a trivalent cation distinct from the divalent cations *e.g.* Al^{3+} as M^{III} and Mg^{2+} as M^{II} for the common hydrotalcite Al–Mg-LDH.[5] But it is possible to synthesize such a structure using only one metallic element. This is well known for iron, Fe-LDH, also known as "green rust"[6,7] or "fougerite".[8,9] Sulfate Fe-LDH is very active in reducing nitrate[10] or other pollutants.[11] This mono-metallic layered structure is also observed for cobalt,[12,13] forming single transition metal hydroxides with mixed valences. The monometallic Co-LDH can be used as capacitors with high pseudo-capacitive performance[14] or for the oxygen evolution reaction. In addition, cerium monometallic LDHs exist with interesting photocatalytic properties[15] but because of the high oxidation state of Ce (Ce^{3+}–Ce^{4+}), sulfate ions are not simply in the interlayer space but also directly connected to the cerium. Other lanthanide-LDHs have also been synthesized.[16]

Manganese is frequently incorporated into LDH structures as a divalent cation with Al^{3+} (ref. 17–19) or as a trivalent cation with Mg^{2+}, Zn^{2+} or Co^{2+} (ref. 20–23) because of its photocatalytic potential.[24] These LDHs can be used for phototherapy against cancers,[25] for the electrocatalytic detection of hydrogen peroxide[23] or as an electrode for the oxygen evolution reaction.[26] However, to our knowledge, it was never used as a single metallic constituent of LDH. One of the main limitations is the impossibility to obtain a stable Mn^{3+} solution excluding the classical coprecipitation method using an initial solution prepared by the dissolution of Mn^{II} and Mn^{III} salts. The Mn^{III} cations contained in the LDH were obtained either by introducing an oxidant such as H_2O_2 in the initial solution[27] or probably due to the contact of the LDH suspension with air.[28,29]

Besides coprecipitation, another pathway for the synthesis of LDH is the oxidation of M^{II} hydroxide. $Mn(OH)_2$ oxidation was thoroughly studied half a century ago[30] and it appeared that the formation of oxide (Mn_3O_4), birnessite[31] or oxide-hydroxide MnO(OH) was the sole fate. However, a new Mn^{II} salt was discovered recently with sulfate in its structure.[32] In this article, this salt was successfully transformed into Mn-LDH with sulfate anions in the interlayer space.

The possibility to stabilise a mixed Mn^{II}–Mn^{III} species in a hydroxide structure opens new perspectives because of their redox properties. Indeed, soluble $Mn^{2+}_{(aq)}$ species are well known to be very slowly oxidised by soluble oxygen in acidic or

[a]Université de Lorraine, CNRS, LCPME, F-54000 Nancy, France.
E-mail: damien.cornu@univ-lorraine.fr, christian.ruby@univ-lorraine.fr
[b]Université Clermont Auvergne, Clermont Auvergne INP, CNRS, ICCF, F-63000 Clermont-Ferrand, France
[c]Université de Strasbourg, CNRS, IPCMS, F-67000 Strasbourg, France
[d]Université de Lorraine, CNRS, CRM2, F-54000 Nancy, France

neutral aqueous solutions. Mn^{II} species present in more compact solid structures such as spinels (*e.g.* hausmannite) are well known to be stable in contact with air. In contrast, hydroxylated Mn^{II} species present in an open solid structure such as LDH are expected to be much more reactive. Such differences in reactivity were clearly demonstrated in the case of Fe^{II} containing compounds, *i.e.*, the oxidation of $Fe(OH)_2$ or Fe_3O_4 by NO_3^- is extremely slow in comparison to the nitrate oxidation of Fe-LDH.[33] Finally, the existence of a mixed Mn^{II}–Mn^{III} LDH structure has to be considered when analysing the oxidation of Mn^{II} in geology. Indeed, the source of Mn^{III} in aqueous media is still debated.[34]

Results

Oxidation of manganese hydroxide sulfate solution

Firstly, $Mn_4(OH)_6SO_4$ or $Mn(OH)_2$ was produced by adding 1 mol L^{-1} NaOH solution into 0.4 mol L^{-1} $MnSO_4$ solution. The ratio $R = \frac{n(OH^-)}{n(Mn^{2+})}$ indicates the proportion of the NaOH amount in the solutions. For R values below 1.5, $Mn_4(OH)_6SO_4$ is produced,[32] while $Mn(OH)_2$ was produced for higher R values. As long as the solids obtained for various R values with $MnSO_4$ are kept under nitrogen bubbling, the suspensions remain white while their pH values are stable for hours.

For a given R value, $Na_2S_2O_8$ solution is then added drop by drop. Subsequently, the solids darken upon the addition of the oxidant (ESI Fig. S1†) except for $R = 0$ (no addition of OH^-). This is in agreement with the fact that Mn^{2+} is not oxidized because of the large free energy barrier to overcome.[35] The pH value decreases upon $S_2O_8^{2-}$ addition (ESI Fig. S2†).

The R value is now fixed at 1.5 in order to maximise the amount of initial $Mn_4(OH)_6SO_4$. The progress of the addition of $S_2O_8^{2-}$ in the solution is defined by the parameter $x = \frac{2n(S_2O_8^{2-})}{n(Mn^{2+})}$. According to the stoichiometry of the oxidation reaction, if the reaction is complete, then x is also equal to the fraction of the Mn^{III} valence in the Mn^{II} and Mn^{III} mixture as one persulfate accepts two electrons to produce sulfate ions.

Fig. 1 indicates the pH and the potential E_h/SCE for increasing x values. Three different zones can be observed: the A zone ends with the inflection for $x = 0.266$ (inflection point for other R values are discussed in ESI section 2†), the B zone, in which one can observe a pseudo-plateau for E_h and pH, and the C zone with a final drop.

For various x values, we analysed the remaining quantities of aqueous cations and anions in solution. Quantities are indicated in Fig. 2 and were measured by inductively coupled plasma mass spectrometry (aqueous Mn species) and ion chromatography (SO_4^{2-}).

4 possible chemical reactions between $Mn_4^{II}(OH)_6SO_4$ and the oxidant are listed below:

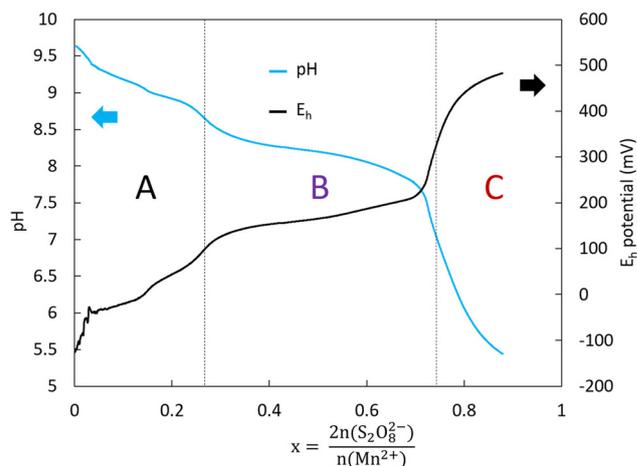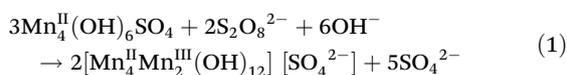$$3Mn_4^{II}(OH)_6SO_4 + 2S_2O_8^{2-} + 6OH^- \\ \rightarrow 2[Mn_4^{II}Mn_2^{III}(OH)_{12}][SO_4^{2-}] + 5SO_4^{2-} \quad (1)$$

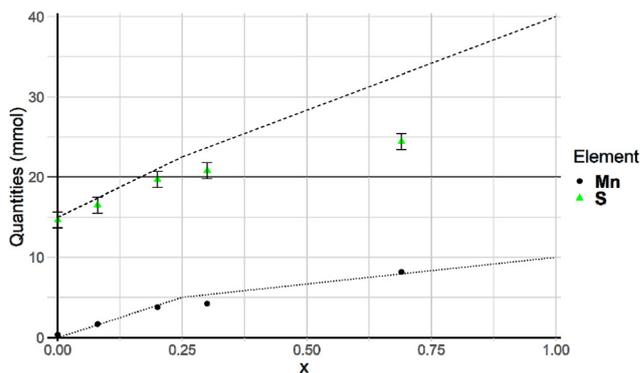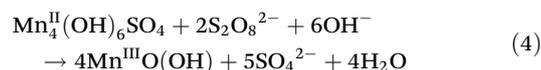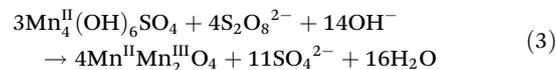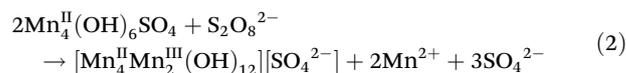Fig. 1 pH and E_h/silver chloride electrode values for a R = 1.5 $MnSO_4$ solution as a function of x.

Fig. 2 Soluble Mn (black circles) and SO_4^{2-} (green triangles), from ICP-MS measurement and ion chromatography, respectively, for R = 1.5 $MnSO_4$ solution as a function of the x ratio. Error bars for Mn are smaller than the mark (0.1 mmol). Dotted lines show the expected quantities in solution for the formation of Mn-LDH through eqn (2) for x between 0 and 0.25 and then the transformation of this solid into MnO(OH) for x between 0.25 and 1 (For interpretation of the references to colour in this figure legend, the reader is referred to the Web version of this article.).

$$2Mn_4^{II}(OH)_6SO_4 + S_2O_8^{2-} \\ \rightarrow [Mn_4^{II}Mn_2^{III}(OH)_{12}][SO_4^{2-}] + 2Mn^{2+} + 3SO_4^{2-} \quad (2)$$

$$3Mn_4^{II}(OH)_6SO_4 + 4S_2O_8^{2-} + 14OH^- \\ \rightarrow 4Mn^{II}Mn_2^{III}O_4 + 11SO_4^{2-} + 16H_2O \quad (3)$$

$$Mn_4^{II}(OH)_6SO_4 + 2S_2O_8^{2-} + 6OH^- \\ \rightarrow 4Mn^{III}O(OH) + 5SO_4^{2-} + 4H_2O \quad (4)$$

Eqn (1) and (2) describe the formation of a new type of LDH containing only Mn (Mn-LDH) equivalent to the green rust (Fe-LDH) which presents a Fe^{II}/Fe^{III} ratio of 2. Water molecules within the Mn-LDH are omitted for the moment in the chemical formula that will be written as $Mn_4^{II}Mn_2^{III}(OH)_{12}SO_4^{2-}$. For eqn (1), the entire Mn atoms are incorporated in the solid, which is not in agreement with what is observed

in Fig. 2. This possibility is therefore rejected. For eqn (2), there is a simultaneous release of Mn^{2+} cations in the solution. Eqn (3) and (4) describe the formation of the well-known mixed oxide $Mn^{II}Mn_2^{III}O_4$ and oxyhydroxide $Mn^{III}O(OH)$.

For x values lower than 0.25, the remaining quantities of Mn and sulfate in the solution are in clear agreement with the expected values from eqn (2). In addition, the stability of the pH during this phase indicates that there is little consumption of OH^- in this reaction. Besides, the inflections for other R values are also in agreement with this stoichiometry (ESI section 2†). For $x = 0.25$, the maximum quantity of Mn-LDH is obtained.

For values between 0.25 and 0.75, the pseudo-plateau in the pH values can be attributed to the transformation of Mn-LDH into MnO(OH) (as determined by XRD in the next section) as in eqn (5). The oxidation reaction of Mn-LDH does not involve any change in the acid–base concentrations:

$$[Mn_4^{II}Mn_2^{III}(OH)_{12}][SO_4{}^{2-}] + S_2O_8{}^{2-}$$
$$\rightarrow 4Mn^{III}O(OH) + 2Mn^{2+} + 3SO_4{}^{2-} + 4H_2O \quad (5)$$
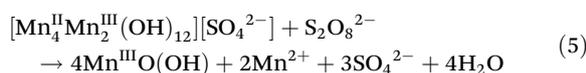
Again, the remaining quantity of Mn in solution is in agreement with this chemical reaction. However, the quantity of sulfate is much lower than what is predicted. It is therefore very likely that, along with MnO(OH) and Mn_3O_4, an additional solid precipitate was also formed. The large peak for the sulfate vibrations in Raman for $R = 1.00$ (Fig. 4) is in agreement with this hypothesis.

It is interesting to note that the production of the fully oxidized metal(III) oxyhydroxide species is also observed for further oxidation of Co[14] and Fe[36] monometallic LDHs.

Eqn (2) and (5) together indicate that half of the initial manganese is released as Mn^{2+} cations that cannot be oxidized under our conditions (ESI p.4†). Oxidation to Mn_3O_4 is also possible and observed during the degradation of Mn-LDH in contact with air.

Characterization of the oxidation products

XRD. Mn-LDH formation in the previous section is proposed due to stoichiometric considerations. The X-ray diffractograms of the wet solids produced for $R = 1.5$ and various x values are presented in Fig. 3. For $x = 0$, pyrochroite ($Mn(OH)_2$) and $Mn_4(OH)_6SO_4$[32] patterns are observed, which is no longer the case for $x = 0.12$ (Fig. 3). Instead, a similar basic Mn^{II} salt is observed: $[Mn(OH)_2]_7[MnSO_4]_2 \cdot H_2O$. This structure was also observed upon drying $Mn_4(OH)_6SO_4$.[32] Alongside this structure, other diffraction peaks are present which are then the only ones to be observed for $x = 0.24$. The XRD pattern for $x = 0.24$ is characteristic of layered LDH compounds with the first $(00l)$ diffraction peaks indicating an interlayer distance of about 11 Å. A Le Bail (profile matching) mode of refinement using the usual space group for LDH compounds, which is the $R\bar{3}m$ trigonal space group with the a_0 planar lattice parameter close to 3.2 Å clearly indicated the absence of a rhombohedral network (ESI Fig. S4a†). A second attempt based on the $P\bar{3}m1$ space group corresponding to the brucite like $Mn(OH)_2$ crystal
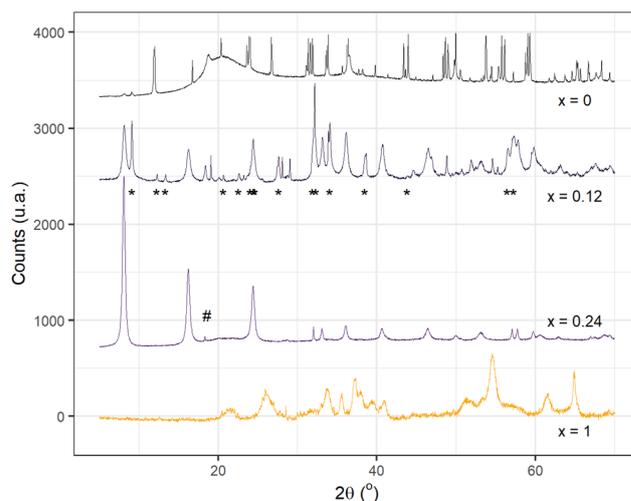
Fig. 3 XRD of the solids obtained from $MnSO_4$ solution with $R = 1.5$ for various x ratios. Stars represent the main peaks for the $[Mn(OH)_2]_7[MnSO_4]_2 \cdot H_2O$ structure (JCPDS file 00-018-0788). # indicates the additional peak due to the Mn-LDH superstructure.

structure[37] led to a reliable refinement with the following hexagonal refined unit cell parameters: $a_0 = 3.2270(7)$ Å and $c = 10.9390(23)$ Å (indexation is shown in ESI Fig. S4b†). The refinement obtained was relevant although one low intensity diffraction peak (close to 18.3°, see # on Fig. 3) was not considered, suggesting the presence of a superstructure. Similar to the Fe-LDH phase intercalated with $SO_4{}^{2-}$,[37] a superstructure in the basal plane with $a = \sqrt{3}\, a_0$ and the $P\bar{3}1m$ space group was tested. The obtained Le Bail simulation was improved by including all the diffraction signals (ESI Fig. S4c†). The definitive refined unit cell parameters are as follows: $a = 5.5917 (1)$ Å and $c = 10.9492 (4)$ Å, very close to those reported for the Fe-LDH phase intercalated with $SO_4{}^{2-}$:[38] $a = 5.5524 (1)$ Å and $c = 11.011 (3)$ Å.

For $x = 1$, the diffractogram shows larger peaks that can be attributed to poorly crystalline manganite γ-MnO(OH) and groutite α-MnO(OH).

Vibrational spectroscopy. The evolution of Raman spectra of the wet structures for $R = 1,5$ and increasing the x amount of persulfate are shown in Fig. 4. For the $x = 0$ spectrum, the pyrochroite identified in XRD corresponds to the peak at 637 cm^{-1}, as referenced in the RRUFF database R10004.[39] The other main peak at 525 cm^{-1}, as well as the sharp sulfate peak at 997 cm^{-1}, indicates the presence of $Mn_4(OH)_6SO_4$.[32] For $x = 0.24$, two peaks at 431 and 523 cm^{-1} are observed, corresponding to the $E_u(T)$ and the $A_{1g}(T)$ vibrations in LDH.[40] Those values are close to what is measured with the sulfate Fe-LDH (427 and 518 cm^{-1}),[8] which suggest the presence of only one solid.

As the oxidation continues, a broad peak centered at around 592 cm^{-1} emerges. This peak can be attributed to the vibrations of a mixture of α-MnO(OH) at 550 cm^{-1} (ref. 41) and γ-MnO(OH) (558 cm^{-1} for the symmetric stretching of the Mn–O–Mn bridge and 621 cm^{-1} for the asymmetric stretching of

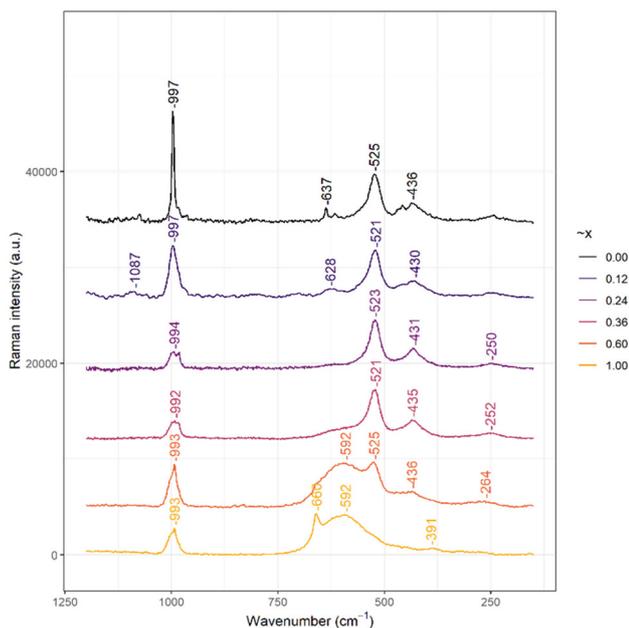**Fig. 4** Raman spectra of the wet solids obtained using the R = 1.5 manganese sulfate solution for increasing x values.

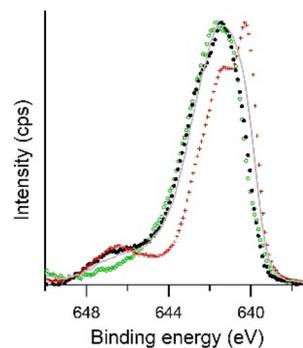**Fig. 5** XPS in the Mn $2p_{3/2}$ region of the solids for R = 1.5 and x = 0.24 ratios (black dots), x = 1 (green open dots), and Mn(OH)$_2$ (red cross), as well as their combination (grey line), are plotted.

these bridges).[42] It is noteworthy that the oxidation of the solid is not homogeneous and pure LDH as well as pure MnO(OH) spots can be found while translating the laser spot on the x = 0.6 solid.

The last spectrum for x = 1 shows no more vibration associated with the LDH, and a new peak emerges at 660 cm^{-1} which can be attributed to the Mn$_3$O$_4$,[41] structure that was not observed in XRD.

Infrared spectroscopy confirms the transformation of the basic salt into LDH, with both compounds containing sulfate anions in their structure, followed by subsequent oxidation to oxide and oxide-hydroxide (ESI section 3.2†).

XPS. XPS is performed on the dried product. Unfortunately, the attempts to wash the solid to remove sodium sulfate impurities were not successful as the solid degraded in pure water solution. Using XPS, we were able to measure the proportion of the dried solid that is sodium sulfate using the relative proportion of oxygen, manganese, sulfur, and sodium. In this dry unrinsed sample, we found that 25% of the mass is Na$_2$SO$_4$, which is consistent with the Na$_2$SO$_4$ concentration measured in the preparation medium. The remaining mass is in agreement with the formula Mn$_6$(OH)$_{12}$SO$_4$·8H$_2$O.

In Fig. 5, Mn $2p_{3/2}$ features the results from the contributions of various Mn valence states. Due to the coupling between the unpaired electrons of the outer shell and unpaired core electron resulting from photoionization, high spin Mn ions give rise to multiplet splitting. Overlapping of these multiplets poses a serious difficulty for qualitative and quantitative analysis of the Mn valence state.[43–52] Fig. 5 shows the Mn $2p_{3/2}$ peak at 642.0 eV with a shoulder at 643 eV, which suggests the coexistence of Mn^{II} and Mn^{III} valence states. The

shake-up satellite at 646 eV appears as the fingerprint of Mn^{II} in MnO,[44–46] LDH,[48] or Mn(OH)$_2$ as shown in Fig. 5. The Mn $2p_{3/2}$ spectra of Mn(OH)$_2$ and MnO(OH) (Mn^{III}) as well as their linear combination with an area ratio of 38 : 62 were added as shown in Fig. 5. The latter fairly reproduces the spectrum of Mn-LDH confirming the mixed-valence Mn^{II}–Mn^{III} nature of this compound, even if it fails to account for the expected Mn^{II}/Mn^{II} ratio of 2.

O 1s, S 2p and valence band spectra are given in ESI section 3.4.†

Thermogravimetric measurements. Thermogravimetric analysis (TGA) of the dried powder was performed (ESI Fig. S9†). Two weight losses were observed, at 95 and 174 °C, which is again in the same range as that observed for Fe-LDH[38] (117 and 153 °C), which can be attributed to the vaporization of slightly bonded water molecules present in the interlayer and to the condensation reaction between hydroxyl groups in the hydroxide sheets and their departure as water molecules, respectively. Those mass losses (13.5 and 8%, respectively, of the total mass) correspond respectively to 18% and 10.5% of the LDH mass in the dried product determined by XPS analysis (75% of the dried product is Mn-LDH). This indicates that there are 8 water molecules per unit slightly bonded in the dried structure (8.5 in the Fe-LDH) and 4.5 additional water molecules leave at higher temperatures because of the condensation of 9 hydroxyl groups (2 water molecules and 4 hydroxyl groups for the Fe-LDH) associated with the formation of MnO(OH) and Mn$_2$O$_3$ at higher temperatures. This indicates that the complete structure of the solid is Mn$_6$(OH)$_{12}$SO$_4$·8 H$_2$O.

Magnetic properties. The susceptibility was recorded under a 0.5 T dc field (ESI Fig. S10†) as a function of temperature.

The Curie constant, determined from the fit of the $1/\chi = f(T)$ curve using the Curie–Weiss law, is C = 18.7 emu K mol^{-1} (Fig. 6). This value is in the same order of magnitude as the one expected from the elemental formula, oxidation degrees, and composition of the solid phase (23.5 emu K mol^{-1} considering a high-spin configuration for Mn^{II} and Mn^{III} with g = 2). The negative Weiss temperature, θ = −105 K, indicates the occurrence of predominant antiferromagnetic interactions.
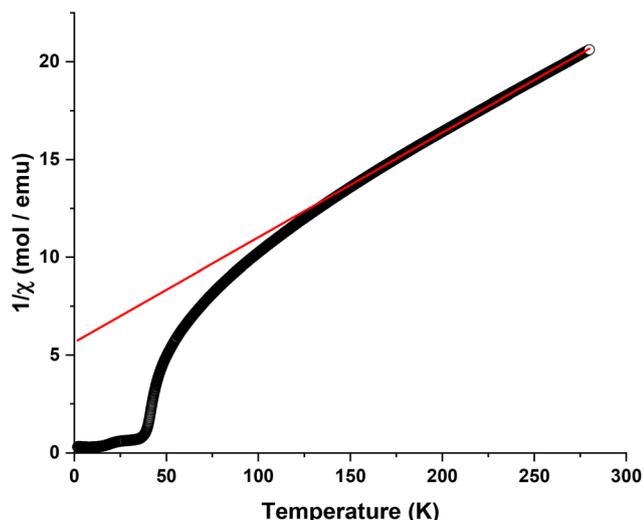
Fig. 6 $1/\chi = f(T)$ (black circles) for compound LDH-Mn, under a dc field of 0.5 T and the best fit of the high temperature region (>150 K) using the Curie–Weiss law (full red line).
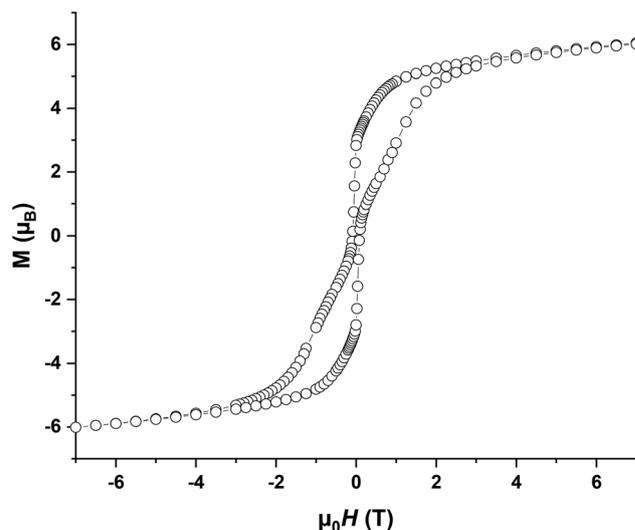

Fig. 7 $M = f(H)$ at 1.8 K.

The χT product (ESI Fig. S10†) decreases when the temperature decreases slowly down to a minimum at 67 K (9.2 emu K mol^{-1}). Then, the χT product increases sharply to two successive maxima, at 33.5 K and 16.2 K (49.3 and 44.7 emu K mol^{-1} respectively). This overall behavior points to the occurrence of ferrimagnetic ordering, with two magnetic phases. One hypothesis to explain the presence of two magnetic phases can be the existence of phases with different hydration levels, which may modify the interaction between the layers, and hence the magnetic coupling leading to different ordering temperatures.

The magnetic ordering is better evidenced by ac susceptibility measurements, performed under a zero dc field, and a 2 Oe oscillating field (ESI Fig. 11†). These measurements reveal a rather complex ordering phenomenon, with five peaks in the out-of-phase susceptibility (at 39.5, 37.4 (shoulder), 14.2, 6.1 and 2.0 K).

None of these peaks are frequency dependent, which exclude the signature of potential small paramagnetic clusters with slow magnetic relaxation. Therefore, ac measurements evidence five ferro or ferrimagnetic ordering temperatures, likely corresponding to the presence of five magnetic phases, and not only two as evidenced by dc measurements. This distribution of ordering temperatures is not unusual for layered hydroxide based magnets;[53–55]

Finally, magnetization *vs.* field at a low temperature (1.8 K) is presented in Fig. 7. At a high field, the magnetization varies linearly with the field and is far from the expected value for a full spin alignment, as expected for a ferrimagnetically ordered material. The coercive field is 88 mT at 1.8 K.

SEM. Scanning electron microscopy was also used to characterize Mn-LDH (Fig. 8). Some ribbon structures can be seen, with 0.5 μm width, a few μm length and 0.1 μm thickness. This kind of structure could not be seen in the Mn$_4$(OH)$_6$SO$_4$ salt (ESI Fig. S5†). This ribbon structure is different from what
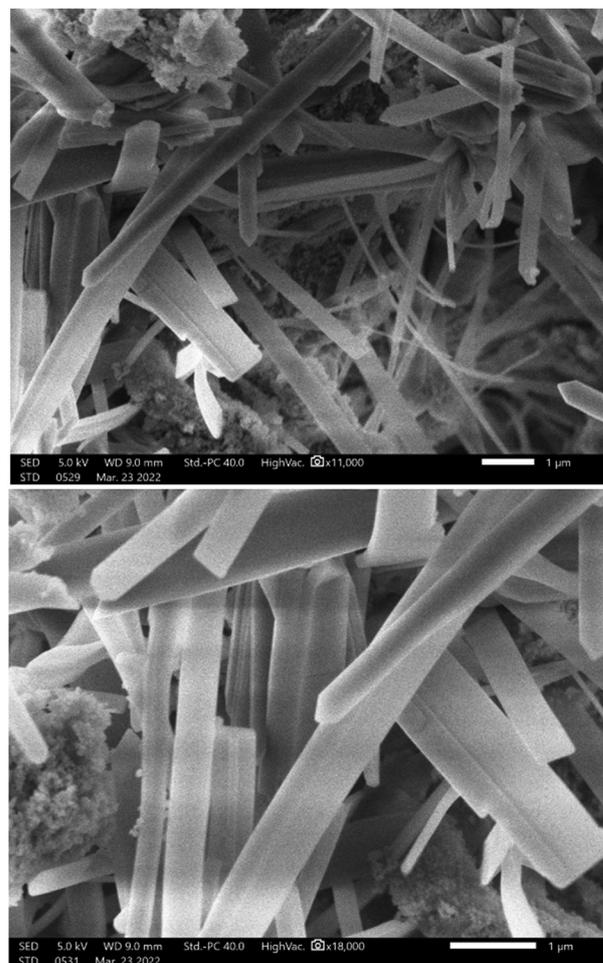

Fig. 8 SEM images of Mn-LDH obtained for $x = 0.25$.

is observed for Fe[56] and Co-LDH,[13] in which a hexagonal morphology was reported in SEM. The small roundish shapes of residual crystallites could be attributed to the part of the LDH oxidized in Mn_3O_4.

The preferential direction for the growth of Mn-LDH could be related to the anisotropy created by the Jahn–Teller effect in the Mn^{III} octahedron,[57] even if this effect could not be seen in the Rietveld analysis.

Discussion

Structure of the obtained product

Chemical analysis of the solution, as well as the variations of the pH (ESI section 2†) during the oxidation of $Mn_4(OH)_6SO_4$, shows that the stoichiometry of the reaction is compatible with the formation of Mn-LDH with a chemical composition of $Mn_2^{III}Mn_4^{II}(OH)_{12}SO_4 \cdot xH_2O$. X-ray diffraction and Raman spectroscopy show similar results for the Fe- and Mn-LDH intercalated by sulfate. Thermogravimetric analysis indicates that 8 water molecules are present in the interlayer space for each Mn-LDH motif based on two Mn^{2+}, leading to the formula: $Mn_2^{II}Mn_4^{III}(OH)_{12}SO_4 \cdot 8H_2O$. The XRD pattern was therefore treated by Rietveld refinements using the structural data of Fe-LDH intercalated by sulfate as a starting point. This initial structural model was efficient, and refinement cycles were carried out. Careful work has been done on the refinement of the diffraction peak profile, using anisotropic size parameters linked to the platelet shaped LDH crystallites. In the course of refinement the d_{S-O} interatomic distances for sulfate anions were fixed at the 1.55 (1) Å value with a regular tetrahedral shape. Fig. 9 shows the obtained Rietveld plot and Table 1

**Table 1** Refined structure of Mn-LDH

Parameters	Mn-LDH (SO_4^{2-})
Space group	$P\bar{3}1m$
Lattice parameters	$a = 5.58821 (9)$ Å
	$c = 10.9410 (4)$ Å
Atomic positions	
Mn^{3+} (1a)	(0 0 0)
Mn^{2+} (2c)	($\frac{2}{3}$ $\frac{1}{3}$ 0)
OH^- (6k)	(0.327(3) 0 0.0935(6))
H_2O (12l)	(−0.248(3) 0.564(2) 0.6624(5))
S^{6+} (2e)	(0 0 0.6054(8))
O_A^{2-} (2e)	(0 0 0.7481(7))
O_B^{2-} (6k)	(0.275(2) 0 0.573(1))
Site occupancies	
H_2O (12l)	0.39(3)
Sulfate (2e)	0.25(−)
Reliability factors	
R_{Bragg}	0.031
R_F	0.060
R_p	0.027
R_{wp}	0.036
R_{exp}	0.026

shows the refined structural parameters of the Mn-LDH compound compared with those of the Fe-LDH analog (ESI Table 2†).

The origin of this ordering is in the interlayer in which sulfate anions are located at specific positions apical to trivalent Mn^{3+} cations. Having a Mn^{3+}/SO_4^{2-} ratio of 2 explains the formation of double planes within the interlayer; each Mn^{3+} octahedron being bounded only to one sulfate anion by a single face of the main layer (Fig. 10). The rest of the interlayer region is occupied by relatively mobile water molecules, and the refined occupancy for water molecules on the Wyckoff site corresponds to the following chemical composition: $Mn_2^{III}Mn_4^{II}(OH)_6 \cdot SO_4 \cdot 9H_2O$, close to the one deduced by thermo-
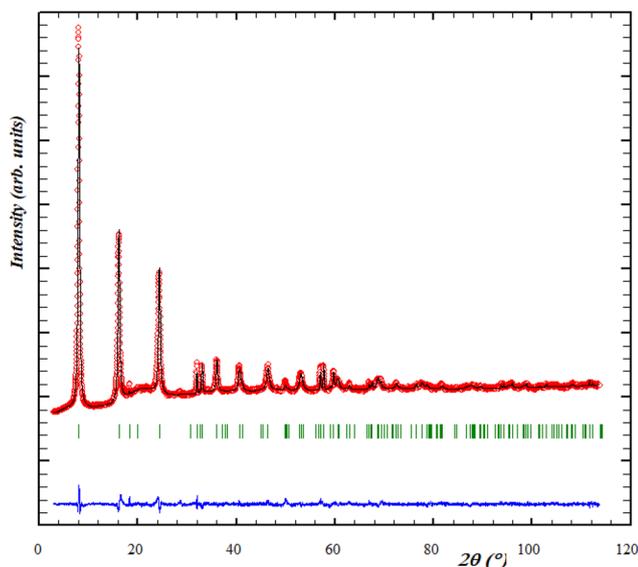
Fig. 9 Rietveld plot for the refined structural model of the Mn-LDH compound intercalated with sulfate anions showing the diffraction measured pattern (red dots), the calculated pattern (black line), the difference curve (blue line) and sticks for the Bragg peak positions.
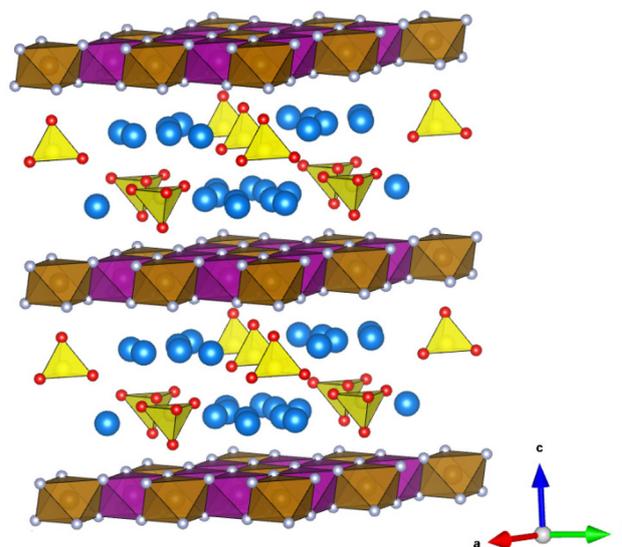
Fig. 10 Representation of the Mn-LDH crystal structure. Main layers composed of Mn^{3+} (brown) and Mn^{2+} (purple) octahedra, intercalated by sulfate anions (yellow tetrahedra) and water molecules (blue spheres).

gravimetric analysis ($Mn_2^{III}Mn_4^{II}(OH)_6 \cdot SO_4 \cdot 8H_2O$) Fig. 10 presents the crystal structure of the Mn-LDH synthesized compound. The superstructure of this sulfate intercalated Mn-LDH phase along the [110] direction of the $Mn(OH)_2$ basic structure[37] allows the ordering of the divalent and trivalent manganese cations, respectively, in the 2c and 1a Wyckoff positions (Table 1) which impose a Mn^{2+}/Mn^{3+} ratio of 2.

Redox properties

The redox potential E_h for the oxidation of $\{Fe(OH)_{2(s)}, Fe^{2+}_{(aq)}\}$ solution by air was used to determine the standard Gibbs free energy of Fe-LDH.[38] For example, a value $\Delta_f G^0$(Fe-LDH) = -3790 ± 10 kJ mol^{-1} was determined by this method for Fe-LDH with sulfate in good agreement with other works.[58] Unfortunately, as the basic salt $Mn_4(OH)_6SO_4$ is not referenced, the first step of oxidation (A part of Fig. 1) transforming it into Mn-LDH cannot be used to determine its standard Gibbs free energy of formation: $\Delta_f G^0$(Mn-LDH) value.

In contrast, the redox potential values recorded in zone B ($0.4 < x < 0.7$) were relatively constant and a pseudo E_h plateau was observed. Zone B corresponds to the transformation of the Mn-LDH into MnO(OH). In fact, the product is a mixture of manganite γ-MnO(OH) and groutite α-MnO(OH). The value E^0(MnO(OH)/Mn-LDH) = +1.117 V/SHE was computed (ESI section 3.1†) by using the experimental E_h/ESH value (+380 mV) and pH value (8.2) recorded in the middle of the E_h plateau of zone B and corrected with the relative silver chloride electrode potential (Fig. 1).

By using the $\Delta_f G^0$ values reported in ESI Table S4,† the standard Gibbs energy of formation of $Mn_4^{II}Mn_2^{III}(OH)_{12}SO_4$ was estimated to be in between -4519 and -4436 kJ mol^{-1}, the lower and the higher values being determined for the final oxidation products manganite or groutite, respectively. The Pourbaix diagrams of Fe and Mn species were built by using the standard chemical potential of ESI Table S4† and the Nernst equations of the relevant redox couples with the details of the calculations in section 4.1.

The reduction reaction of nitrate to either ammonium or dinitrogen by oxidizing Fe-LDH to γ-FeO(OH) is thermodynamically favorable. Previously performed experiments are in agreement with such a prediction and Fe-LDH was observed to reduce nitrate either in ammonium[10] for sulfate and chloride containing Fe-LDH or into a mixture of ammonium and N-gaseous species for carbonate containing LDH.[59]

Interestingly, the limit between the domain of stability of nitrate and dinitrogen is still situated above the one separating MnO(OH) and Mn-LDH on the Mn-Pourbaix diagram (Fig. 11A), while it is not the case for the line separating nitrate and ammonium/ammonia. This means that Mn-LDH is not reactive enough to reduce nitrate into ammonium, but it may potentially reduce nitrate into N_2. This is in line with what is observed in the manganese assisted denitrification process in a laboratory scale sequencing batch reactor by Swathi et al.[60]

The latter reaction is of utmost importance if the goal is to find a material useful for the water denitrification process.
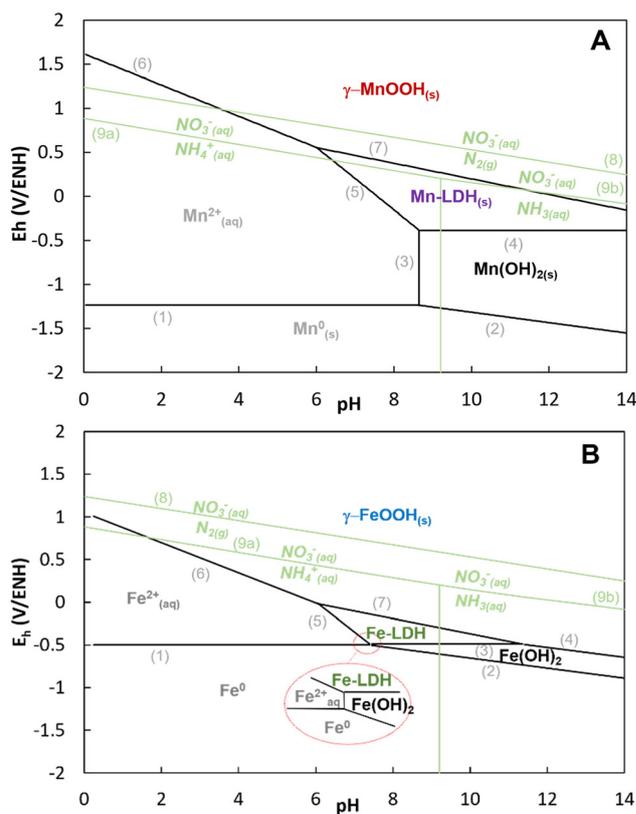

Fig. 11 Pourbaix diagrams for Mn (A) and Fe (B).

Such properties could be unique among the monometallic LDH family. Indeed, Fe-LDH is a too strong reductant that transformed nitrate mainly into the more reduced form of nitrogen, i.e. NH_4^+. In contrast, Co-LDH and Ni-LDH could be too weak reductants to transform NH_4^+ into N_2. Such a preliminary forecast can be proposed by comparing similar redox potentials, e.g. the standard potentials E^0 of $M^{2+}_{(aq)}/M_2^{III}O_{3(s)}$ redox couples are equal to 0.728, 1.443, 1.746 and 1.753 V/SHE when M = Fe, Mn, Co and Ni, respectively.[61] However, further experiments dedicated to the determination of the standard chemical potentials of Co-LDH and Ni-LDH and to the reactivity of monometallic LDH towards nitrate species should be explored to confirm these assumptions.

Conclusions

A new monometallic manganese double layered hydroxide $Mn_2^{III}Mn_4^{II}(OH)_6 \cdot SO_4 \cdot 8H_2O$ was discovered using $Mn_4^{II}(OH)_6SO_4$ oxidation with $S_2O_8^{2-}$ and following the pH, E_h and composition of the liquid solution during the oxidation. The characterization (XRD, Raman, infrared, and thermogravimetric analysis) of the solid shows that the structure of Mn-LDH is very close to the one of Fe-LDH (green rust). XPS shows that the solid contains a mixture of Mn^{II} and Mn^{III}, which is confirmed by magnetic experiments. SEM shows a ribbon shape organization of the solid, perhaps linked with a preferential direction

due to the Jahn–Teller effect induced by Mn^{III} ions. The crystal structure was therefore determined using Rietveld refinement. The solid was determined to be ferrimagnetic at low temperatures.

Pourbaix diagrams calculated from the experimental measurements during the synthesis indicate that this solid is theoretically able to reduce nitrate into dinitrogen without further reduction to ammonium or ammonia. This indicates that this solid could be used for water remediation. Finally, the eventual formation of Mn-LDH in the natural environment should also be considered. Indeed, fougerite, the mineral containing Fe-LDH, is already identified in hydromorphic soils and groundwater. Mn^{II}–Mn^{III} LDH could be an intermediate species in the oxidation pathway of manganese.

Experimental

Synthesis

Mn-LDH were synthesized using 50 mL of $MnSO_4 \cdot H_2O$ (Sigma Aldrich, >99%) solution (0.4 mol L^{-1}) with a variable volume of 1 mol L^{-1} NaOH (VWR 31627.290) to reach the desired R value $\left(R = \dfrac{n(OH^-)}{n(Mn^{2+})} \right)$ under stirring and nitrogen bubbling. Once the pH was stabilized, a 0.2 mol L^{-1} solution of $Na_2S_2O_8$ (Sigma Aldrich, >99%) was added using a peristaltic pump with a flow of 0.167 mL min^{-1} and the pH and the redox potential E_h were registered with a Metrohm pH electrode Unitrode with Pt1000 and a Toledo Inlab redox electrode. The x value indicates the quantity of persulfate introduced, as $x = \dfrac{2n(S_2O_8{}^{2-})}{n(Mn^{2+})}$. For XPS analysis, $Mn(OH)_2$ was prepared from a mixture of 1.12 g of $MnCl_2 \cdot 4H_2O$ (Sigma Aldrich, >98%) and 0.57 g of NaOH (VWR, 99.1%) in 40 ml of water under nitrogen bubbling.

Characterization studies

ICP-MS. Released manganese concentrations in the solution were measured by Inductively Coupled Plasma Mass Spectroscopy (ICP-MS, Agilent-7800). 100 μL of the supernatant solution after centrifugation was diluted to 100 mL with water. The calibration curve in the range 50–2000 ppb has been established using Sigma-Aldrich 74128 samples. The detected isotope was ^{55}Mn.

Ion chromatography. Sulfate concentration was determined by ion chromatography. Analysis was performed with a Metrohm 882 Compact IC plus instrument equipped with chemical (Metrohm suppressor MSM II) and sequential (Metrohm CO2 suppressor MCS) suppressors and a conductimetric detector. The eluent (1.8 mmol L^{-1} Na_2CO_3 and 1.7 mmol L^{-1} $NaHCO_3$ solution) flowed continuously through a Metrosep A Supp 4–250/4.0 column associated with a guard column (Metrosep A supp 4/5 guard). Standard solutions were prepared from commercial 1000 μg mL^{-1} anions (Merck 1.11448.0500). The flow rate and the injected volume were respectively 1 mL min^{-1} and 20 μL.

XRD. The products were measured soon after their synthesis and centrifugation. XRD diffractograms were recorded either on a wet sample (x = 0, 0.12 and 0.24) or on the sample dried under nitrogen flow (x = 1). For the wet sample, excess water was removed by pressing the water soaked paste between tissues. The resulting paste was measured on an approximately 10 μm thick zero background X-ray holder covered with a minimal amount of glycerol to protect the paste from air oxidation, as the compounds were known to be air sensitive. Multiple (at least 15) 1 h X-ray scans were collected, and the diffractograms did not show any sign of evolution, the multiple scans were summed up for better X-ray statistics.

Powder X-ray diffraction patterns were recorded with a Panalytical X'Pert Pro MPD diffractometer in reflection geometry using a tube with Cu radiation ($K_{\alpha1}$ = 1.5406 Å, a Ge(111) incident-beam monochromator, 0.02 rad Soller slits, programmable divergence and antiscatter slits (the irradiated area was fixed to 10 mm × 10 mm)), and an X'Celerator detector. Data were collected from finely ground samples with a sample holder spinner and continuous rotation of the sample to improve the statistical representation of the sample.

XPS. X-ray photoelectron spectra were recorded on a KRATOS Axis Ultra Xray photoelectron KRATOS Axis Ultra DLD spectrometer equipped with a monochromated Al K_α source ($h\nu$ = 1486.6 eV, spot size 0.7 mm × 0.3 mm). The detector was a hemispherical analyzer at an electron emission angle of 90° and a pass energy of 20 eV (high resolution spectra). For the high-resolution spectra, the overall energy resolution, resulting from the monochromator and electron analyzer bandwidths, was higher than 800 meV. The C 1s binding energy of adventitious carbon was taken as 284.6 eV. O 1s spectra were decomposed using Gaussian peaks after using the Shirley method of background subtraction.

Vibrational spectroscopy. Infrared IR measurements of the wet solids were recorded under nitrogen flow in an attenuated total reflectance mode on a Bruker Tensor 27 spectrometer equipped with a KBr beam splitter and a deuterated triglycine sulfate (DTGS) thermal detector. Spectra were recorded and processed using OPUS 7.5 software (Bruker, Karlsruhe, Germany).

10 μL samples for Raman spectra were collected and dried over an aluminium plate. Then Raman spectra were recorded on a Renishaw inVia Qontor microspectrometer equipped with a confocal microscope and an Olympus X50 objective (N.A = 0.55). It should be noted that a nitrogen atmosphere was used to avoid exposure to oxygen. A 532 nm exciting radiation was used with a laser power below 0.05 mW for all samples to prevent their degradation. The spot area was a few μm^2. Several locations were probed on each sample. The spectral resolution was about 4 cm^{-1} and the precision on the wavenumber was lower than 1 cm^{-1}.

SQUID. Magnetic measurements were performed at the Institut de Physique et Chimie des Matériaux de Strasbourg (UMR CNRS-Unistra 7504) using a Quantum Design MPMS3 magnetometer. Magnetization measurements at different fields at a given temperature confirm the absence of

ferromagnetic impurities. Data were corrected for the sample holder and diamagnetism was estimated from Pascal constants.

Thermogravimetric measurements. TGA was performed on a TG/ATD 92-16.18 SETARAM instrument. About 50 mg were introduced into the cell under 2 L h^{-1}Ar with 2° min^{-1} ramp from 20 to 600 °C. The mass loss was corrected with a reference analysis performed using a second heating ramp.

SEM. Scanning Electron Microscopy (SEM) analysis was performed on a JEOL JSM-IT500HR, with a Field Emission Gun (FEG). The powder sample was fixed on double face scotch tape. The analysis was made under high vacuum, and we settled on a 60 μm diaphragm aperture. The voltages for analysis were from 2 kV to 5 kV. We used mainly the Secondary Electron Detector (SED) for imaging the powder.

Author contributions

DC: Conceptualization, investigation, writing – original draft, and writing – review & editing; RC, GRo, and GRe: investigation and writing – review & editing; PD and AR: investigation; CC and CR: writing – review & editing.

Data availability

Most of the data and figures of this publication were deposited in the DOREL database: **https://dorel.univ-lorraine.fr/dataset.xhtml?persistentId=doi:10.12763/TLLN2F**

Conflicts of interest

There are no conflicts to declare.

Acknowledgements

Notes and references

1 Z. Cai, X. Bu, P. Wang, J. C. Ho, J. Yang and X. Wang, *J. Mater. Chem. A*, 2019, **7**, 5069–5089.

2 G. Zhang, X. Zhang, Y. Meng, G. Pan, Z. Ni and S. Xia, *Chem. Eng. J.*, 2020, **392**, 123684.

3 M. Zubair, M. Daud, G. McKay, F. Shehzad and M. A. Al-Harthi, *Appl. Clay Sci.*, 2017, **143**, 279–292.

4 Y. Kuthati, R. K. Kankala and C.-H. Lee, *Appl. Clay Sci.*, 2015, **112–113**, 100–116.

5 M. V. Bukhtiyarova, *J. Solid State Chem.*, 2019, **269**, 494–506.

6 W. Feitknecht and G. Keller, *Z. Anorg. Allg. Chem.*, 1950, **262**, 61–68.

7 J. D. Bernal, D. R. Dasgupta and A. L. Mackay, *Clay Miner. Bull.*, 1959, **4**, 15–30.

8 F. Trolard, J.-M. R. Génin, M. Abdelmoula, G. Bourrié, B. Humbert and A. Herbillon, *Geochim. Cosmochim. Acta*, 1997, **61**, 1107–1111.

9 C. Ruby, A. Géhin, R. Aissa and J.-M. R. Génin, *Corros. Sci.*, 2006, **48**, 3824–3837.

10 H. Chr, B. Hansen, C. B. Koch, H. Nancke-Krogh, O. K. Borggaard and J. Sørensen, *Environ. Sci. Technol.*, 1996, **30**, 2053–2056.

11 M. Usman, J. M. Byrne, A. Chaudhary, S. Orsetti, K. Hanna, C. Ruby, A. Kappler and S. B. Haderlein, *Chem. Rev.*, 2018, **118**, 3251–3304.

12 Z. P. Xu and H. C. Zeng, *Int. J. Inorg. Mater.*, 2000, **2**, 187–196.

13 R. Ma, K. Takada, K. Fukuda, N. Iyi, Y. Bando and T. Sasaki, *Angew. Chem.*, 2008, **120**, 92–95.

14 P. Vialat, C. Mousty, C. Taviot-Gueho, G. Renaudin, H. Martinez, J.-C. Dupin, E. Elkaim and F. Leroux, *Adv. Funct. Mater.*, 2014, **24**, 4831–4842.

15 T. Ye, W. Huang, L. Zeng, M. Li and J. Shi, *Appl. Catal., B*, 2017, **210**, 141–148.

16 J. Liang, R. Ma, F. Geng, Y. Ebina and T. Sasaki, *Chem. Mater.*, 2010, **22**, 6001–6007.

17 L.-M. Grand, S. J. Palmer and R. L. Frost, *J. Therm. Anal. Calorim.*, 2010, **100**, 981–985.

18 T. Coelho, R. Micha, S. Arias, Y. E. Licea, L. A. Palacio and A. C. Faro, *Catal. Today*, 2015, **250**, 87–94.

19 C. Yang, L. Liao, G. Lv, L. Wu, L. Mei and Z. Li, *J. Colloid Interface Sci.*, 2016, **479**, 115–120.

20 S. Bhattacharjee and J. A. Anderson, *Adv. Synth. Catal.*, 2006, **348**, 151–158.

21 Y. Du, Q. Wang, X. Liang, Y. He, J. Feng and D. Li, *J. Catal.*, 2015, **331**, 154–161.

22 J. M. Fernandez, C. Barriga, M.-A. Ulibarri, F. M. Labajos and V. Rives, *J. Mater. Chem.*, 1994, **4**, 1117–1121.

23 H. Farhat, C. Taviot-Gueho, G. Monier, V. Briois, C. Forano and C. Mousty, *J. Phys. Chem. C*, 2020, **124**, 15585–15599.

24 Z. Timár, G. Varga, S. Muráth, Z. Kónya, Á. Kukovecz, V. Havasi, A. Oszkó, I. Pálinkó and P. Sipos, *Catal. Today*, 2017, **284**, 195–201.

25 Y. Ruan, X. Jia, C. Wang, W. Zhen and X. Jiang, *Chem. Commun.*, 2018, **54**, 11729–11732.

26 F. Song and X. Hu, *J. Am. Chem. Soc.*, 2014, **136**, 16481–16484.

27 X. Zhao, C. Niu, L. Zhang, H. Guo, X. Wen, C. Liang and G. Zeng, *Chemosphere*, 2018, **204**, 11–21.

28 R. Li, Y. Liu, H. Li, M. Zhang, Y. Lu, L. Zhang, J. Xiao, F. Boehm and K. Yan, *Small Methods*, 2019, **3**, 1800344.

29 X. Wang, H. Yan, J. Zhang, X. Hong, S. Yang, C. Wang and Z. Li, *J. Alloys Compd.*, 2019, **810**, 151911.

30 R. Scholder and H. Kyri, *Z. Anorg. Allg. Chem.*, 1952, **270**, 56–68.

31 H. Boumaiza, R. Coustel, G. Medjahdi, C. Ruby and L. Bergaoui, *J. Solid State Chem.*, 2017, **248**, 18–25.

32 D. Cornu, R. Coustel, P. Durand, C. Carteret and C. Ruby, *J. Solid State Chem.*, 2021, **305**, 122631.

33 C. J. Matocha, P. Dhakal and S. M. Pyzola, in *Advances in Agronomy*, ed. D. L. Sparks, Academic Press, 2012, vol. 115, pp. 181–214.

34 C. M. Hansel, in *Advances in Microbial Physiology*, ed. R. K. Poole, Academic Press, 2017, vol. 70, pp. 37–83.

35 S. Namgung, C.-M. Chon and G. Lee, *Geosci. J.*, 2018, **22**, 373–381.

36 P. Refait, C. Bon, L. Simon, G. Bourrie, F. Trolard, J. Bessiere and J. M. R. Genin, *Clay Miner.*, 1999, **34**, 499–510.

37 A. N. Christensen and G. Ollivier, *Solid State Commun.*, 1972, **10**, 609–614.

38 L. Simon, M. François, P. Refait, G. Renaudin, M. Lelaurain and J.-M. R. Génin, *Solid State Sci.*, 2003, **5**, 327–334.

39 B. Lafuente, R. T. Downs, H. Yang and N. Stone, in *Highlights in Mineralogical Crystallography*, ed. T. Armbruster and R. M. Danisi, DE GRUYTER, Berlin, München, Boston, 2015, pp. 1–30.

40 A. Di Bitetto, *Thèse: Etude structurale et dynamique d'hydroxydes doubles lamellaires: du matériau carbonaté aux hybrides organo-minéraux*, 2017.

41 B. Hu, K. Lu, Q. Zhang, X. Ji and W. Lu, *Comput. Mater. Sci.*, 2017, **136**, 29–35.

42 P. F. Smith, B. J. Deibert, S. Kaushik, G. Gardner, S. Hwang, H. Wang, J. F. Al-Sharab, E. Garfunkel, L. Fabris, J. Li and G. C. Dismukes, *ACS Catal.*, 2016, **6**, 2089–2099.

43 A. A. Audi and P. M. A. Sherwood, *Surf. Interface Anal.*, 2002, **33**, 274–282.

44 E. S. Ilton, J. E. Post, P. J. Heaney, F. T. Ling and S. N. Kerisit, *Appl. Surf. Sci.*, 2016, **366**, 475–485.

45 M. C. Biesinger, B. P. Payne, A. P. Grosvenor, L. W. M. Lau, A. R. Gerson, R. St. and C. Smart, *Appl. Surf. Sci.*, 2011, **257**, 2717–2730.

46 H. W. Nesbitt and D. Banerjee, *Am. Mineral.*, 1998, **83**, 305–315.

47 H. Jung and Y.-S. Jun, *Environ. Sci. Technol.*, 2016, **50**, 105–113.

48 M. Asif, W. Haitao, D. Shuang, A. Aziz, G. Zhang, F. Xiao and H. Liu, *Sens. Actuators, B*, 2017, **239**, 243–252.

49 J. O. Eniola, R. Kumar, A. A. Al-Rashdi, M. O. Ansari and M. A. Barakat, *ACS Omega*, 2019, **4**, 18268–18278.

50 S. Werner, V. W. Lau, S. Hug, V. Duppel, H. Clausen-Schaumann and B. V. Lotsch, *Langmuir*, 2013, **29**, 9199–9207.

51 T. Li, J. Wang, Y. Xu, Y. Cao, H. Lin and T. Zhang, *ACS Appl. Energy Mater.*, 2018, **1**, 2242–2253.

52 A. N. Simonov, R. K. Hocking, L. Tao, T. Gengenbach, T. Williams, X.-Y. Fang, H. J. King, S. A. Bonke, D. A. Hoogeveen, C. A. Romano, B. M. Tebo, L. L. Martin, W. H. Casey and L. Spiccia, *Chem. – Eur. J.*, 2017, **23**, 13482–13492.

53 F. Bellouard, M. Clemente-León, E. Coronado, J. R. Galán-Mascarós, C. J. Gómez-García, F. Romero and K. R. Dunbar, *Eur. J. Inorg. Chem.*, 2002, **2002**, 1603–1606.

54 E. Coronado, J. R. Galán-Mascarós, C. J. Gómez-García and V. Laukhin, *Nature*, 2000, **408**, 447–449.

55 Q. Evrard, Z. Chaker, M. Roger, C. M. Sevrain, E. Delahaye, M. Gallart, P. Gilliot, C. Leuvrey, J.-M. Rueff, P. Rabu, C. Massobrio, M. Boero, A. Pautrat, P.-A. Jaffrès, G. Ori and G. Rogez, *Adv. Funct. Mater.*, 2017, **27**, 1703576.

56 I. A. M. Ahmed, L. G. Benning, G. Kakonyi, A. D. Sumoondur, N. J. Terrill and S. Shaw, *Langmuir*, 2010, **26**, 6593–6603.

57 S. Hirai, S. Yagi, A. Seno, M. Fujioka, T. Ohno and T. Matsuda, *RSC Adv.*, 2015, **6**, 2019–2023.

58 K. B. Ayala-Luis, C. B. Koch and H. C. B. Hansen, *Clays Clay Miner.*, 2008, **56**, 633–644.

59 M. Etique, A. Zegeye, B. Grégoire, C. Carteret and C. Ruby, *Water Res.*, 2014, **62**, 29–39.

60 D. Swathi, P. C. Sabumon and S. M. Maliyekkal, *Int. Biodeterior. Biodegrad.*, 2017, **119**, 499–510.

61 J. Van Muylder and M. Pourbaix, *Atlas d'équilibres électrochimiques*, Gauthier-Villars & Cie, Paris, 1963, p. 378.